Measurement of cross-magnetic-field heat transport due to long-range collisions*

E. M. Hollmann,[†] F. Anderegg, and C. F. Driscoll

*Physics Department and Institute for Pure and Applied Physical Sciences,
University of California at San Diego, La Jolla, California 92093*

Cross-magnetic-field heat transport in a quiescent pure ion plasma is found to be diffusive and to be dominated by long-range ''guiding center'' collisions. In these long-range collisions, which occur in plasmas with Debye length λ_D greater than cyclotron radius r_c, particles with impact parameters $r_c < \rho \lesssim \lambda_D$ exchange parallel kinetic energy only. The resulting thermal diffusivity χ_L is independent of magnetic field B and plasma density n. The measured thermal diffusivity χ agrees within a factor of 2 with the long-range prediction $\chi_L = 0.49 n \bar{v} b^2 \lambda_D^2$ over a range of 1000 in temperature, 50 in density, and 4 in magnetic field. This thermal diffusivity is observed to be up to 100 times larger than classical diffusivity from short-range velocity-scattering collisions. These long-range collisions are typically dominant in unneutralized plasmas, and may also contribute to electron heat transport in neutral plasmas. © *2000 American Institute of Physics.*
[S1070-664X(00)93205-1]

I. INTRODUCTION

The study of cross-magnetic-field heat transport in plasmas is an area of active research relevant to magnetic fusion plasmas,[1] astrophysical objects,[2] plasma processing,[3] and basic plasma physics.[4] Heat transport can be broadly categorized as collisional or turbulent. ''Collisional'' transport is driven by the fluctuating fields from thermal motions of individual particles, whereas ''turbulent'' transport is driven by nonthermal fluctuations such as unstable waves or broadband turbulence. This paper treats collisional transport only.

Collisional transport can occur as a result of direct (binary) Coulomb collisions and as a result of wave-mediated (multiple-particle) collisions. Direct Coulomb collisions between particles can occur over distances up to a Debye shielding length λ_D, while wave-mediated collisions can occur over distances as large as the plasma dimensions. In a direct Coulomb collision, the character of the collision depends on the impact parameter ρ compared to the cyclotron radius r_c; here, we distinguish between ''short-range'' collisions, with impact parameters $\rho \lesssim r_c$ and ''long-range'' collisions, with impact parameters $r_c < \rho \lesssim \lambda_D$. In theory, short-range collisions occur in all plasmas, while long-range collisions occur only in plasmas with $r_c < \lambda_D$.[5]

''Classical'' transport theory analyzes short-range collisions with $\rho \lesssim r_c$. These collisions cause scattering between the perpendicular and parallel velocities, and thus drive the perpendicular and parallel velocity distributions toward a Maxwellian with a single temperature T. For ion–ion collisions, the (momentum transfer) collision rate[6] resulting from short-range collisions is

$$\nu_{ii} = \frac{16}{15} \sqrt{\pi} n \bar{v} b^2 \ln\left(\frac{r_c}{b}\right) \approx (1.0 \text{ s}^{-1}) T^{-3/2}$$
$$\times n_7 [1 + 0.08 \ln(T^{3/2} B^{-1})], \quad (1)$$

where $b \equiv e^2/T$ is the distance of closest approach and $\bar{v} \equiv \sqrt{T/m}$ is the ion thermal velocity. Here, the numerical values are appropriate to $^{24}\text{Mg}^+$ ions, with density $n_7 \equiv n/10^7 \text{ cm}^{-3}$, magnetic field B in Tesla and temperature T in eV. Equation (1) uses the form of the Coulomb logarithm appropriate for plasmas with $r_c < \lambda_D$,[7] where $r_c \equiv \bar{v}/\Omega_c \approx (0.5 \text{ mm}) T^{1/2} B^{-1}$ and $\lambda_D \equiv [T/4\pi e^2 n]^{1/2} \approx (2.4 \text{ mm}) T^{1/2} n_7^{-1/2}$. These collisions cause a random cross-field step of the ion guiding centers by a distance of order r_c, causing cross-field diffusion of particles, momentum, and heat. The resulting classical thermal diffusivity χ_c is predicted[8] to be

$$\chi_c = \nu_{ii} r_c^2 \approx (2.5 \times 10^{-3} \text{ cm}^2 \text{ s}^{-1}) T^{-1/2}$$
$$\times B^{-2} n_7 [1 + 0.08 \ln(T^{3/2} B^{-1})]. \quad (2)$$

In contrast, ''long-range'' transport occurs as a result of collisions with impact parameters $r_c < \rho < \lambda_D$. In these long-range collisions, the ions exchange parallel energies over radial distances ρ. The interaction time is long compared with the cyclotron orbit time of the particles, so the cyclotron action $\mu_\perp \equiv m v_\perp^2 / 2B$ of each particle is conserved and there is no significant change in the perpendicular velocities. There is also a small $\mathbf{E} \times \mathbf{B}$ drift during these collisions; this produces negligible heat transport, but is important for particle and angular momentum transport.[5] The cross-field thermal diffusivity χ_L resulting from long-range collisions is calculated[9] to be

$$\chi_L = 0.49 n \bar{v} b^2 \lambda_D^2 \approx (1.1 \times 10^{-3} \text{ cm}^2 \text{ s}^{-1}) T^{-1/2}. \quad (3)$$

This long-range thermal diffusivity χ_L results from collisions between pairs of particles with small relative parallel velocity $\Delta v \lesssim (b/\lambda_D)\bar{v}$; pairs of particles with large relative velocities do not exchange parallel velocities in these one-dimensional collisions. The number density of these particles is $\Delta n \simeq (b/\lambda_D)n$, so the resulting collision rate scales as $\nu \propto \Delta v \Delta n \lambda_D^2$ and the thermal diffusivity scales as $\chi_L = \nu \lambda_D^2 \propto \Delta n \Delta v \lambda_D^2 \lambda_D^2 \propto n\bar{v}b^2\lambda_D^2$, as in Eq. (3).

Comparing Eqs. (2) and (3) suggests that long-range heat transport will be larger than short-range heat transport in plasmas with $\lambda_D \gtrsim 7r_c$. Single species plasmas are commonly in this regime due to the Brillouin density limit,[10] and the electrons in some neutral plasmas are in this regime, i.e., $\lambda_D \gtrsim 7r_{ce}$.

Wave-mediated collisions are predicted to occur as a result of the thermal emission and absorption of lightly damped plasma waves over distances $\rho \gg \lambda_D$. In low-collisionality plasmas, the resulting cross-field thermal diffusivity is expected to scale as[11]

$$\chi_w \propto n\bar{v}b^2\lambda_D L_T, \tag{4}$$

where L_T is the scale length of the thermal gradient. Wave-mediated heat transport is thus expected to be dominant in plasmas with very large thermal gradient length scales, i.e., $L_T \gg \lambda_D$. It is estimated[9] that the wave-mediated thermal diffusivity of Eq. (4) will be larger than the long-range collisional thermal diffusivity of Eq. (3) if $L_T \gtrsim 100\lambda_D$. However, the present experiments have $L_T < 100\lambda_D$.

Overall, we expect a cross-field heat flux Γ_q given by

$$\Gamma_q = -\tfrac{5}{2}n(\chi_L \nabla T_\parallel + \chi_c \nabla T) + \Gamma_{ND}, \tag{5}$$

where the term Γ_{ND} represents a possible heat flux due to higher-order temperature gradients or due to nondiffusive effects such as waves or convection. In Eq. (5), we have separately identified $T_\parallel$ to emphasize the unusual nature of χ_L, but for most of our experiments we have $T_\perp \simeq T_\parallel \equiv T$.

Here, we measure collisional heat transport in a quiescent pure ion plasma.[12] Quiescent plasmas with a single sign of charge (nonneutral plasmas) are used for a wide range of basic plasma physics and atomic physics experiments.[13] These plasmas are routinely confined in a near-thermal equilibrium state where fluctuation levels are small and transport is dominated by collisions, rather than by turbulent processes. The present measurements are made on uncorrelated magnesium–ion (Mg^+) plasma columns with temperatures $5 \times 10^{-4} < T < 0.5$ eV, densities $0.2 < n_7 < 10$, and magnetic fields $1 < B < 4$ T. The measurements show that the cross-magnetic-field heat flux in these plasmas is diffusive, i.e., $\Gamma_{ND} \simeq 0$, with average thermal diffusivity $\chi \approx 1.7\chi_L \gg \chi_c$. These measurements are consistent with the theory perspective given above: here, the thermal diffusivity is expected to be dominated by long-range collisions, since $\lambda_D \gg r_c$. Also, the derivation[9] of χ_L in Eq. (3) presumes that $L_T > \lambda_D$, which is reasonably well satisfied in the experiments. Wave-mediated transport is not expected to be significant in the present experiments, since $L_T \lesssim 100\lambda_D$.
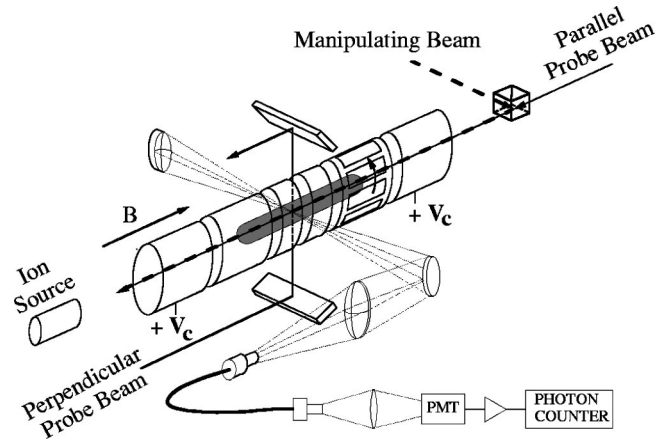

FIG. 1. Cylindrical ion trap with ''manipulating'' and ''probe'' laser beams.

II. EXPERIMENTAL SETUP

The experimental apparatus is shown schematically in Fig. 1. Magnesium ions are created with a metal vacuum vapor arc (MEVVA)[14] and are trapped in a Penning-Malmberg trap with uniform axial magnetic field B (i.e., $\Delta B/B \lesssim 10^{-3}$), and end-confinement voltages $V_c = 200$ V. Electrons initially created by the MEVVA are not confined by the end voltages and therefore leave the trap in an axial transit time. Typically, $N_{tot} \approx 5 \times 10^8$ ions form a plasma column of length $L_p \approx 14$ cm and radius $R_p \approx 0.5$ cm inside conducting cylinders with radius $R_w = 2.86$ cm. These plasmas consist of about 70% Mg^+, with the remainder being mostly magnesium hydrides, MgH_n^+, formed when ions interact with the residual neutral background gas (H_2) at pressure $P \approx 4 \times 10^{-9}$ Torr.

The radial electric field due to the (totally unneutralized) ion charges causes the plasma column to $\mathbf{E} \times \mathbf{B}$ drift rotate at a (central) frequency of $f_E \equiv nec/B \approx (14.4$ kHz$)$ $n_7 B^{-1}$. Diamagnetic and centrifugal drifts are small, so the total fluid rotation frequency is $f_{rot} \approx f_E$. This rotation is rapid compared to the heat transport times discussed here, so our radial transport measurements are effectively azimuthally averaged. Individual thermal ions bounce axially at a rate $f_b \equiv \bar{v}/2L_p \approx (7.1$ kHz$)$ $T^{1/2}(L_p/14$ cm$)^{-1}$, so axial transport is rapid compared with radial transport and we can assume the plasma to be uniform along the magnetic field lines. The plasma is uncorrelated, with the ion–ion correlation parameter $10^{-4} \lesssim \Gamma \lesssim 1$, where $\Gamma \equiv e^2/aT = (5 \times 10^{-5})n_7^{1/3}T^{-1}$; at lower temperatures, the ions would be in a liquid ($1 \lesssim \Gamma \lesssim 170$) or solid ($\Gamma > 170$) plasma state.[15]

These ion plasmas are quiescent, with density fluctuations of $\delta n/n < 10^{-3}$ estimated from wall sector signals.

The plasmas normally slow their rotation and expand radially on a time scale of $\tau_m \approx 2000$ s due to undesirable ''drags'' from small azimuthal asymmetries in the electric or magnetic confining fields. In the present experiments, we counterbalance these drags with torque from an applied ''rotating wall'' voltage perturbation[16] at frequency $f \gtrsim f_E$; this technique allows the ions to be held in a near-thermal-equilibrium steady state for days or weeks. The heating due to radial expansion (Joule heating) or due to the rotating wall
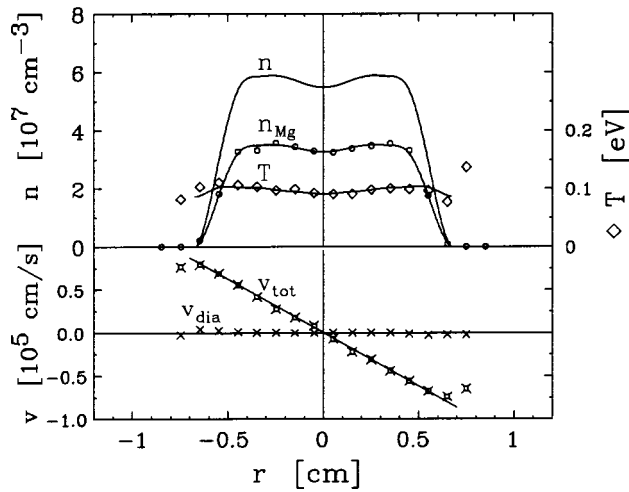
FIG. 2. (a) Measured Mg$^+$ density n_{Mg} and temperature T; and calculated total charge density n as a function of radius r. (b) Measured total fluid rotation v_{tot} and calculated diamagnetic rotation velocity v_{dia}.

FIG. 3. Radial profiles showing steady-state laser-heated (a) and laser-cooled (b) plasmas.

drive is balanced by cooling from collisions with the neutral background gas, and the plasma typically relaxes to an equilibrium at $T \approx 0.05$ eV. Usually, the rotating wall drive is turned off during the heat transport experiments; however, we find that the results obtained for the thermal diffusivity are the same with the rotating wall on or off, as will be discussed in Sec. V.

The plasma density, temperature, and rotation frequency are measured using laser-induced fluorescence (LIF) from a weak ($\approx 10 \mu$W) continuous probe laser beam at $\lambda = 280$ nm. Typically, the probe beam frequency is scanned slowly (1.7 s) through a $3^2 S_{1/2} \rightarrow 3^2 P_{3/2}$ cyclic transition of ^{24}Mg$^+$ at each radial position. The measured ion distribution functions, $f_\perp(v_\perp, r, t)$ and $f_\parallel(v_\parallel, r, t)$ are Maxwellian within experimental accuracy (see Fig. 8 of Ref. 14). From a fit to velocity-shifted Maxwellians, we obtain the local magnesium density $n_{Mg}(r)$, temperatures $T_\perp(r, t)$ and $T_\parallel(r, t)$, and total fluid rotation velocity $v_{tot}(r)$. In the heat transport experiments, the temperature evolution is obtained from a "fast" measurement of just the velocity distribution peaks, that is, $f_\parallel(0, r, t)$ or $f_\perp(v_{tot}, r, t)$; this is sufficient since the ion density is constant during the measurements. As indicated in Fig. 1, the probe beam can be aligned parallel or perpendicular to the magnetic field, and both $T_\perp$ and $T_\parallel$ are measured; for the experiments presented here, however, we can approximate $T_\perp \simeq T_\parallel \equiv T$ to adequate accuracy. The total fluid rotation velocity is $v_{tot}(r) = v_E(r) + v_{dia}(r)$, but the diamagnetic term v_{dia} is generally negligible. Thus, the measured $v_{tot}(r) \approx v_E(r)$ gives the total charge density $n(r)$ through Poisson's equation, i.e., $n(r) = -(B/2\pi ecr)\partial(rv_E)/\partial r$. Typically, we find that $n_{Mg}(r)/n(r) \approx 0.7$ at all radii, so centrifugal mass separation[17] is negligible. The ratio n_{Mg}/n evolves on a very slow ($\approx$ day) time scale which can be neglected in these experiments.

Typical equilibrium plasma profiles are shown in Fig. 2. Here, we display the measured n_{Mg}, T, and v_{tot} versus radius for a plasma that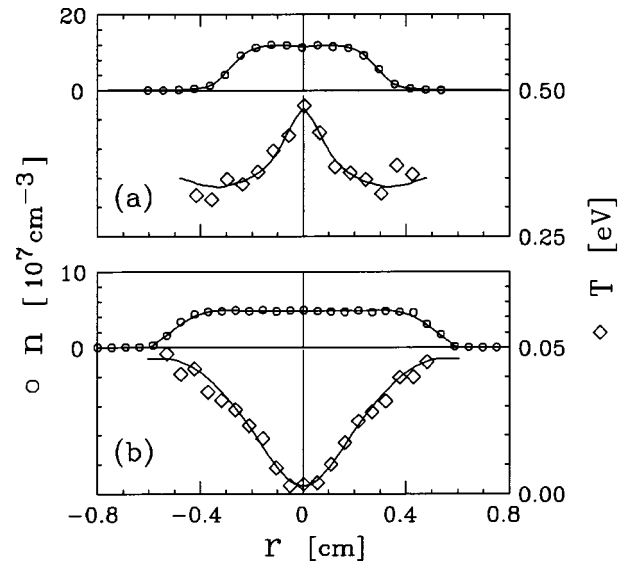 has been held in steady state for 20 h by a rotating wall drive. Also shown is the total charge density n and (negligible) diamagnetic velocity v_{dia} calculated from the measured $n_{Mg}(r)$, $T(r)$. At the two largest radius points ($r = \pm 0.8$ cm), we measure $n \approx 0$, so T and v_{tot} cannot be obtained. These steady-state plasmas are typically confined close to thermal equilibrium, i.e., $n(r)$, $T(r)$, and $f_{rot}(r) \equiv v_{tot}(r)/2\pi r$ are relatively constant over the bulk of the plasma.

A temperature gradient is created in the plasma by locally heating or cooling with a strong (≈ 1mW) manipulating beam at $\lambda = 280$ nm. This heating or cooling is obtained by detuning the parallel manipulating beam to the blue or red side of the cyclic transition. The manipulating beam has a diameter of 1 mm and is aligned along the $r = 0$ axis of the plasma, thus creating an initial condition with a strong radial temperature gradient. The perturbed plasma temperature is assumed to be constant axially, since the plasma is optically thin to the manipulating beam. Azimuthal temperature variations are assumed to be small, since the plasma is spinning rapidly compared with the transport discussed here. The manipulating beam is chopped at 50 Hz and the plasma temperature and density are measured using the probe beam during times when the manipulating beam is off. Examples of steady-state radial profiles of locally heated and cooled plasmas are shown in Fig. 3. Here, the different densities are obtained from different rotating wall drive frequencies f_{rot}. The curves show the smoothing and $\pm r$ symmetrization, which is applied to the measurements before further analysis.

III. RESULTS

Heat transport is measured by creating steady-state plasmas with a strong temperature gradient, such as shown in Fig. 3, then blocking the manipulating beam at time $t = 0$ and measuring the resulting temperature evolution. Here, we use the fast measurement of $f_\parallel(0, r, t)$: the probe beam is tuned to $v_\parallel = 0$, and the LIF counts are accumulated in 10 ms bins, each followed by 30 ms dwell times. Figure 4 shows the
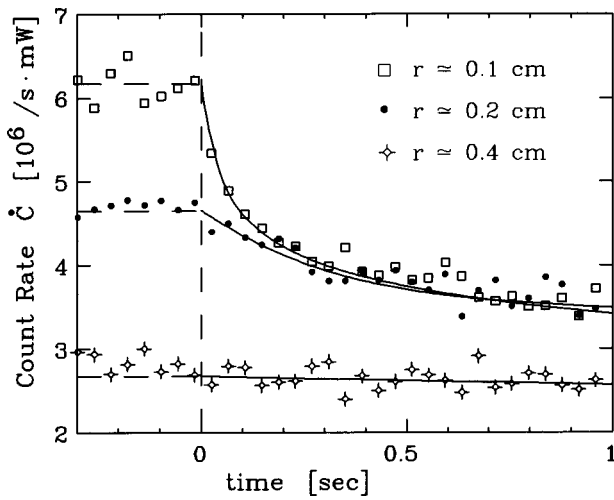
FIG. 4. Measured photon count rate $\dot{C}$ vs time at three radii, as the plasma of Fig. 3(b) relaxes after the cooling is turned off.

FIG. 6. Measured normalized radial heat flux vs temperature gradient for time evolution shown in Fig. 5, demonstrating diffusive heat transport. Data at the three labeled times is shown as bold symbols.

photon count rate $\dot{C}$ measured at three different radii for the initial condition of Fig. 3(b); each time sequence results from a distinct relaxation of the same, repeatable initial condition. The count rate is measured at 100 times $-0.5 < t < 3.5$ s, and is normalized to the (nearly constant) probe beam power at each time step.

The plasma temperature determines the count rate, as $\dot{C} = \alpha f_{\parallel}(0,r,t) \propto n(r)/T_{\parallel}(r,t)^{1/2} \simeq n(r)/T(r,t)^{1/2}$. The constant of proportionality α is determined from the initial steady state $n(r,t \leqslant 0)$ and $T_{\parallel}(r,t \leqslant 0)$, which are known from a slow probe beam frequency scan through the entire distribution function. During the temperature evolution, the density evolves very little, so we approximate $n(r,t) \approx n(r,0)$.

Repeated fast temperature measurements at different radii are used to reconstruct the temperature evolution of the entire plasma, $T(r,t)$. Figure 5 shows the evolution $T(r,t)$ of the initial condition Fig. 3(b) reconstructed from 18 fast temperature measurements such as those shown in Fig. 4. For the purposes of heat flux calculations, we use smooth, radially symmetrized curves fit through the temperature data; curves through the data are shown here at times $t = 0, 0.1,$
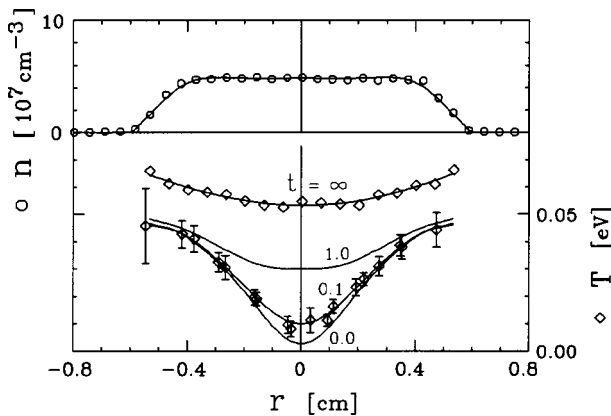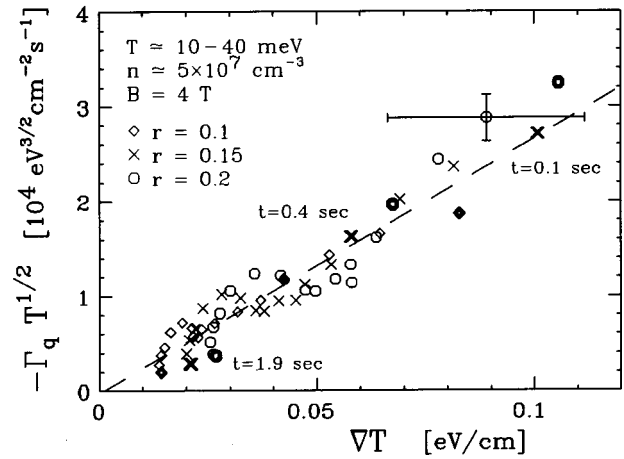

FIG. 5. Measured thermal diffusion starting from locally cooled initial condition of Fig. 3(b).

and 1 s. For clarity, individual temperature data points are shown only at $t = 0.1$ s; the error bars for these points are estimated from the shot noise in the photon counts and from evolution-to-evolution variations in the initially created temperature perturbation. The approximate final equilibrium temperature state $(t \to \infty)$ is also shown; this is measured by leaving the manipulating beam off and letting the plasma relax to an equilibrium with the rotating wall drive left on. The small radial temperature variation seen in the final equilibrium state of Fig. 5 is due to Joule heating (which is largest at large radii) when the rotating wall is off and the plasma is expanding radially; or (equivalently) due to the rotating wall itself when the plasma is macroscopically steady state.

The temperature evolution of Fig. 5 results from a radial heat flux plus small external heating terms. The radial heat flux Γ_q is obtained from the measured change in local energy density, $\dot{q}(r,t) \equiv \partial/\partial t \left[\frac{3}{2} n(r) T(r,t) \right]$ as

$$\Gamma_q(r,t) \equiv -\frac{1}{r} \int_0^r r' \, dr' [\dot{q}(r',t) - \dot{q}_{\text{ext}}(r',t)]. \quad (6)$$

The weak external heating or cooling term $\dot{q}_{\text{ext}}$ is known from independent measurements, as will be described in Sec. IV.

In Fig. 6, we plot the measured radial heat flux Γ_q as a function of the temperature gradient ∇T obtained from the data of Fig. 5. We plot the heat flux measured at radii $r = 0.1, 0.15,$ and 0.2 cm, and at times $t = 0.1 - 1.9$ s. These radii were chosen here because they have a strong gradient and a strong signal, i.e., $\dot{q} \gg \dot{q}_{\text{ext}}$. It can be seen that the gradients and fluxes are largest at early times, and decrease as the temperature profile relaxes toward equilibrium. Since both classical and long-range transport predict $\Gamma_q \propto \chi \nabla T \propto T^{-1/2} \nabla T$, the displayed Γ_q is divided by $T^{-1/2}$ to better illustrate the proportionality with ∇T.

The error bars shown in Fig. 6 follow from the error estimated in Fig. 5; the error shown here is typical of all the data points in Fig. 6. The dashed line in Fig. 6 is an unconstrained, error-weighted linear fit to the data; it can be seen
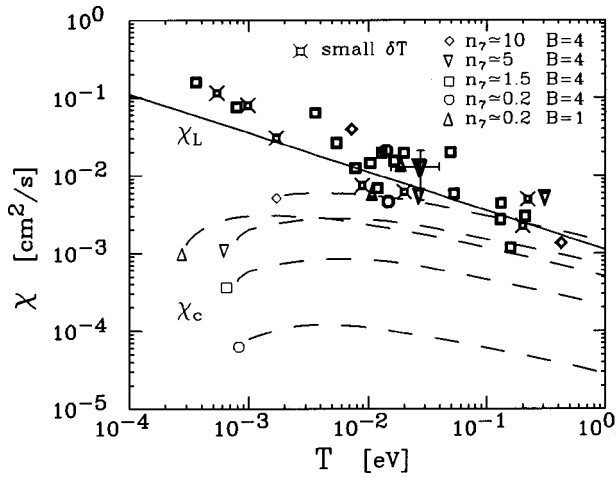
Phys. Plasmas, Vol. 7, No. 5, May 2000

Measurement of cross-magnetic-field heat transport . . .   1771

FIG. 7. Measured cross-magnetic-field thermal diffusivity χ plotted as a function of temperature T, demonstrating heat transport dominated by long-range collisions.

FIG. 8. Measured background heating rate starting from a uniformly cooled initial condition.

that a straight-line fit is a reasonable description of the measurements. The curving trends seen in the late-time points at all three radii are not thought to be significant; here, $\dot{q}$ from heat transport is as small as $\dot{q}_{\text{ext}}$, and inaccuracies in the $\dot{q}_{\text{ext}}$ model result in systematic offsets in Γ_q. Also, from the intercept of the line, it can be seen that $\Gamma_{\text{ND}} \simeq 0$ within the scatter in the data; thus Fig. 6 demonstrates diffusive heat conduction. In general, our measurements show no consistent signature of nondiffusive heat flux.

We calculate the local thermal diffusivity χ for each data point of Fig. 6 using

$$\chi = -\frac{2}{5n} \frac{\Gamma_q}{\nabla T}. \tag{7}$$

Values of $\chi(n, B, T)$ were obtained for different equilibrium plasmas covering a range of 50 in density, 10^3 in temperature, and 4 in magnetic field. In Fig. 7, we plot the measured χ as a function of temperature T. Here, we display a single averaged value of χ for each evolution such as Fig. 6. For example, the data of Fig. 6 give an average thermal diffusivity $\chi \simeq 1.3 \times 10^{-2}$ cm^2 s^{-1}, at an average temperature $T \simeq 0.028$ eV. (This averaging has little consequence, since the range of n, T, and χ in a single evolution is small.) Also shown on one data point are estimated random error bars corresponding to the data of Fig. 6; this level of error is typical of the data shown in Fig. 7. The data points of Fig. 7 labeled ''small δT'' are obtained using a small temperature perturbation about a known equilibrium, as will be described in Sec. V.

The dashed curves in Fig. 7 show the predicted classical thermal diffusivities χ_c for the five densities and magnetic fields used. The solid line shows the predicted long-range thermal diffusivity χ_L, which depends only on temperature. The measured thermal diffusivities are up to 100 times larger than the classical prediction, and are independent of B and n. The $T^{-1/2}$ scaling is observed over 3 decades in T, and extends into the low-temperature regime where $r_c \approx b$. A fit to
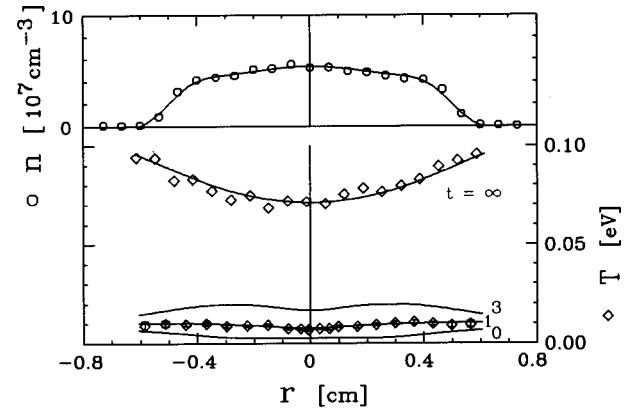
the data with $\chi \propto T^{-1/2}$ gives $\chi = (1.93 \pm 1) \times 10^{-3}$ cm^2 s^{-1} $T^{-1/2} = (0.84 \pm 0.5) \nu \lambda_D^2$, which agrees within a factor of 2 with Eq. (3).

We also verified that the velocity scattering collisions of classical transport are actually occurring at the classical Fokker–Planck rate ν_{ii} of Eq. (1). This velocity scattering rate was measured by inducing anisotropy between $T_\perp$ and $T_\parallel$ and measuring the subsequent rate of temperature isotropization.[18] Since the velocity scattering collisions are not anomalously large, we conclude that the observed strong heat transport must be due to nonvelocity scattering (i.e., long-range) collisions.

IV. BACKGROUND HEATING TERMS

The small external heating correction, $\dot{q}_{\text{ext}}$, used in Eq. (6) is obtained by measuring the temperature evolution of a plasma which has been *uniformly* heated or cooled by a spatially *wide* manipulating beam.

Figure 8 shows such a background heating evolution. The initial steady-state plasma is uniformly cooled to a temperature of $T(r,0) \simeq 3 \times 10^{-3}$ eV. At $t = 0$, the cooling beam is turned off and the subsequent temperature evolution is monitored with a probe beam. For clarity, we show data points only at $t = 1$ s. The evolution is illustrated by smooth fits to the data at the three times $t = 0$, 1, and 3 s, in relation to the approximate final equilibrium temperature $t = \infty$. Here, since radial temperature variations are small, we expect negligible radial heat flux, i.e., $\Gamma_q \approx 0$, implying that $\dot{q} \approx \dot{q}_{\text{ext}}$. As in the heat transport experiments of Sec. III, the rotating wall confinement field is turned off briefly during these measurements. The external heating was measured at $B = 4$ T for a range of parameters: $0.3 < P < 4 \times 10^{-9}$ Torr, $1 < n_7 < 10$, and $10^{-3} < T < 2$ eV.

The background heating measurements are qualitatively consistent with a simple model of Joule heating and neutral gas heating/cooling, i.e.,

$$\dot{q}_{\text{ext}} = \dot{q}_J + \dot{q}_N. \tag{8}$$

Here, the Joule heating is due to the expansion from inherent trap asymmetries. We model this as a uniform density column with $R_p \propto [1+t/\tau_m]^{1/2}$ and $n \propto [1+t/\tau_m]^{-1}$, giving the heating rate

$$\dot{q}_J = -eE_r \frac{nr}{2\tau_m}. \tag{9}$$

The characteristic expansion rate in the regime of these experiments is approximately

$$\tau_m^{-1} \simeq (10^{-3} \ \text{s}^{-1})\left(\frac{B}{4 \ \text{T}}\right)^{-2}\left(\frac{R_p}{0.5 \ \text{cm}}\right)^{-2}. \tag{10}$$

This expansion rate is obtained from measurements over the parameter range $1 \le n_7 \le 14$, $10^{-3} \le T \le 2$ eV, and $0.3 \le R_p \le 0.5$ cm at $B=4$ T and $L_p \simeq 12$ cm. The measured expansion rate does not show the $T^{-1}n^2$ dependence required for the "bounce rigidity" scaling of $(f_b/f_E)^{-2}$ seen in many plasma regimes.[19] This difference may be due to the relatively high collisionality of cold ions: at $T=10^{-3}$ eV and $n_7=1$, for example, we calculate $\nu_{ii}/f_b \simeq 8$, so the ions are actually *diffusing* along the axial magnetic field. We have assumed a B^{-2} expansion rate scaling; this is qualitatively consistent with observed confinement times at different B and also with the $(B/L_p)^{-2}$ scaling seen on most apparatuses.[20] The R_p^{-2} scaling probably relates only to the present experimental techniques for varying n, R_p, and N_{tot}.

The heating (or cooling) expected from ion-neutral (H_2) collisions with relative particle velocity v_{rel} is:

$$\dot{q}_N \simeq -(n_N\sigma_{iN}v_{rel})\frac{2m\,m_N}{(m+m_N)^2}\frac{3}{2}n(T-T_N)$$

$$\simeq -(8.8\times10^4 \ \text{cm}^{-3}\,\text{s}^{-1})(T-T_N)n_7\left(\frac{P}{10^{-9} \ \text{Torr}}\right). \tag{11}$$

Here, T_N is the effective neutral gas temperature seen by the rotating plasma,

$$T_N \equiv 0.026\text{eV} + \tfrac{1}{3}m_N r^2 \omega_E^2$$

$$\simeq 0.026 \ \text{eV}\left[1 + 0.11\left(\frac{r}{1 \ \text{cm}}\right)^2\left(\frac{f_E}{10 \ \text{kHz}}\right)^2\right]. \tag{12}$$

An improved normalization of $\dot{q}_{ext}$ is obtained for each heat-flux experiment such as Fig. 5 by normalizing $\dot{q}_{ext}$ so as to maintain energy conservation in the evolution: that is, we require $\int_0^{R_w} r\,dr\dot{q} = \int_0^{R_w} r\,dr\dot{q}_{ext}$. Typically, we find a normalization factor between 1 and 3, consistent with the factor-of-two uncertainty in the model.

For the heat transport data presented here, the correction to χ due to the external heating terms is small, since $\dot{q}_{ext}/\dot{q} \approx 0.1$ in the regions with a large temperature gradient. The uniformly cooled initial condition of Fig. 8, for example, corresponds to the same conditions on axis ($n \simeq 5\times10^7$ cm^{-3}, $T \simeq 3\times10^{-3}$ eV) as the strong-gradient initial condition of Fig. 5. However, the measured initial heating from background effects on Fig. 8 ($\dot{q}=4\times10^5$ eV cm^{-3} s^{-1}) is
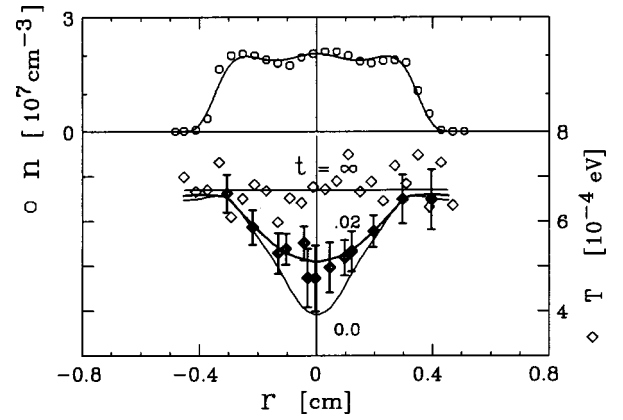

FIG. 9. Measured thermal diffusion starting from small temperature perturbation about a uniformly cooled plasma.

about ten times smaller than the measured initial heating from radial heat flow in Fig. 5 ($\dot{q}=5\times10^6$ eV cm^{-3} s^{-1}). Thus, we have a clear signature of radial heat flow in the data of Fig. 5.

V. SMALL PERTURBATION METHOD

The "small δT" data points in Fig. 7 are obtained by creating small temperature perturbations about a known equilibrium plasma, with the rotating wall kept on during measurements of the subsequent relaxation. We use the terminology "small δT" only to distinguish from the experiments discussed in Sec. III, not to imply that $\delta T \ll T$. This technique allows the external heating terms $\dot{q}_{ext}$ to be estimated by linearizing about the known equilibrium; as will be seen below, the essential assumption here is that the temperature dependence of the external heating terms does not vary with radius. Values of χ are then obtained without the small model-dependent correction introduced by the use of Eq. (8).

A typical "small δT" thermal evolution is shown in Fig. 9. The plasma is held by a steady-state rotating wall drive, and is cooled uniformly with a steady-state cooling beam to a temperature $T(r,\infty) \simeq 7\times10^{-4}$ eV, as shown by the line labeled $t=\infty$. Initially, additional cooling is applied at $r=0$ by a second narrow cooling beam along the axis of the plasma; this results in a central temperature of $T(0,0) \simeq 4\times10^{-4}$ eV, as shown by the curve labeled $t=0$. At $t=0$ the narrow cooling beam is turned off and the plasma temperature relaxes toward the $t=\infty$ equilibrium value. In Fig. 9, the curves are smooth, radially symmetric fits to the temperature data, which is displayed for $t=0.02$ and $t=\infty$, with LIF shot noise error bars shown only for $t=0.02$.

The radial heat flux Γ_q for this experiment is obtained from the measured temperature evolution $T(r,t)$ using Eq. (6), as was done for the large temperature perturbation method described in Sec. III. Here, however, we do not assume that the external heating terms are given by the model Eq. (8); instead we linearize the heating terms about the final equilibrium temperature $T_\infty(r)$:

$$\dot{q}_{ext}(r,T) = \dot{q}_{ext}(r,T_\infty) + \frac{\partial}{\partial T} \dot{q}_{ext}(r,T)\Big|_{T_\infty} \delta T(r,t),$$

$$\equiv \dot{q}_{ext}(r,T_\infty) + \beta(r,t)\,\delta T(r,t), \tag{13}$$

where $\delta T(r,T) \equiv T(r,T) - T_\infty(r)$. Here, we have assumed that the measured equilibrium is steady state; i.e., $\dot{q}_{ext}(r,T_\infty) = 0$. We also have assumed that the radial variation of $\beta(r,t)$ is small over the region where δT is significant; that is, we approximate the external heating terms as being constant in magnitude over the bulk of the plasma. The time variation of $\beta(t)$ is obtained from the data at each time step by using energy conservation: $\beta(t) = (\int r\,dr\,\dot{q})/(\int r\,dr\,\delta T)$. The thermal diffusivity χ is then calculated at each (r,t) as described in Sec. III.

In Fig. 7, each "small δT" data point indicates the average thermal diffusivity obtained for a small perturbation experiment such as Fig. 9. These small temperature perturbation experiments are taken at densities $0.5 \leq n_7 \leq 2.5$ and magnetic fields $1 \leq B \leq 4$ T. It can be seen that the values of χ from the small perturbation method are in good agreement with values of χ obtained using the large perturbation method described in Sec. III.

VI. DISCUSSION

In summary, we have measured the cross-magnetic-field heat flux in a quiescent pure ion plasma. The heat flux is proportional to the thermal gradient ∇T, and is apparently dominated by long-range collisions, predicted to have impact parameters up to 1 Debye length. These long-range collisions cause heat fluxes that are independent of magnetic field strength: the observed thermal diffusivity scales as $\chi \propto n^0 B^0 T^{-1/2}$, as predicted for long-range collisions, whereas the thermal diffusivity resulting from classical, short-range collisions scales as $\chi_c \propto n B^{-2} T^{-1/2}$. At high magnetic field and low densities, the classical prediction is more than two orders of magnitude too small to explain the observed heat fluxes.

This enhanced heat transport should occur in most non-neutral plasmas, where $\lambda_D > r_c$ is always satisfied, and may apply to the electron component of neutral plasmas that satisfy $\lambda_D \gtrsim 7 r_{ce}$. In neutral plasmas, a heat flux that is independent of magnetic field could be significant when scaling to high-field devices.

The enhanced heat transport rate is not caused by the rotating wall drive used here to confine the plasmas in steady state. This can be seen by the agreement in Fig. 7 between the large temperature perturbation data (where the rotating wall is turned off) and the small temperature perturbation method (where the rotating wall is left on). This is intuitively reasonable, since the rotating wall acts to balance radial particle drifts that are extremely slow compared with the observed radial heat transport.

Classical heat transport presumably also occurs in these systems, but it is negligible for most of our parameter range.

Direct measurements of the equipartition rate $\nu_{\perp\parallel} = \frac{1}{2}\nu_{ii}$ between perpendicular and parallel temperatures $T_\perp$ and $T_\parallel$ in these plasmas verify that short-range velocity-scattering collisions are indeed occurring at the rate ν_{ii} of Eq. (1). Presumably, about one half of the heat flux for the high temperature, high density regime in Fig. 7 is due to classical velocity-scattering collisions.

Wave-mediated heat transport is not believed to be significant here, since these plasmas are not sufficiently large; the very lowest-temperature data presented here ($T \simeq 5 \times 10^{-4}$ eV), correspond to plasmas about 100 Debye lengths across. Future experiments will attempt to measure the characteristics of this wave-mediated transport. The possibility of enhanced heat transport due to long-range binary collisions was also considered by Psimopoulos,[21] but questions as to the validity of Debye shielding in 1D suggested impact parameters as large as the skin depth, giving transport magnitudes and scalings substantially different from those observed here.

[1] F. Wagner and U. Stroth, Plasma Phys. Controlled Fusion **35**, 1321 (1993).
[2] S. M. Ichimaru, H. Iyetomi, and S. Tanaka, Phys. Rep. **149**, 93 (1987); B. D. G. Chadran and S. C. Cowley, Phys. Rev. Lett. **80**, 3077 (1998).
[3] M. Tuszewski, Phys. Plasmas **5**, 1198 (1998).
[4] A. T. Burke, J. E. Maggs, and G. J. Morales, Phys. Rev. Lett. **81**, 3659 (1998); D. D. Needleman and R. L. Stenzel, ibid. **58**, 1426 (1987).
[5] D. H. Dubin, Phys. Plasmas **5**, 1688 (1988).
[6] T. M. O'Neil and C. F. Driscoll, Phys. Fluids **22**, 266 (1979).
[7] D. Montgomery, G. Joyce, and L. Turner, Phys. Fluids **17**, 2201 (1974).
[8] M. N. Rosenbluth and A. N. Kaufmann, Phys. Rev. **109**, 1 (1958).
[9] D. H. E. Dubin and T. M. O'Neil, Phys. Rev. Lett. **78**, 3868 (1997).
[10] L. Brillouin, Phys. Rev. **67**, 260 (1945); R. C. Davidson, *Physics of Non-neutral Plasmas* (Addison-Wesley, Redwood City, CA, 1989), p. 42.
[11] M. N. Rosenbluth and C. S. Liu, Phys. Fluids **19**, 815 (1976).
[12] E. M. Hollmann, F. Anderegg, and C. F. Driscoll, Phys. Rev. Lett. **82**, 4839 (1999).
[13] T. M. O'Neil, AIP Conf. Proc. **175**, 1 (1988); J. N. Tan, J. J. Bollinger, and D. J. Wineland, IEEE Trans. Instrum. Meas. **44**, 144 (1995).
[14] F. Anderegg, X.-P. Huang, E. Sarid, and C. F. Driscoll, Rev. Sci. Instrum. **68**, 2367 (1997).
[15] J. H. Malmberg and T. M. O'Neil, Phys. Rev. Lett. **39**, 1333 (1977).
[16] X.-P. Huang, F. Anderegg, E. M. Hollmann, C. F. Driscoll, and T. M. O'Neil, Phys. Rev. Lett. **78**, 875 (1997); F. Anderegg, E. M. Hollmann, and C. F. Driscoll, ibid. **81**, 4875 (1998).
[17] T. M. O'Neil, Phys. Plasmas **24**, 1447 (1981).
[18] F. Anderegg, X.-P. Huang, C. F. Driscoll, E. M. Hollmann, T. M. O'Neil, and D. H. E. Dubin, Phys. Rev. Lett. **78**, 2128 (1997); B. R. Beck, J. Fajans, and J. H. Malmberg, ibid. **68**, 317 (1992).
[19] J. M. Kriesel, Experiments on viscous and asymmetry-induced transport in magnetized, pure electron plasmas, Ph.D. dissertation, UCSD, 1999.
[20] C. F. Driscoll, K. S. Fine, and J. H. Malmberg, Phys. Fluids **29**, 2015 (1986).
[21] M. Psimopoulos and D. Li, Proc. R. Soc. Lond. A **437**, 55 (1992).